

Multi-shape graph-cuts and its application to lung segmentation from a chest CT volume

Keita Nakagomi¹, Akinobu Shimizu¹, Hidefumi Kobatake¹,
Masahiro Yakami², Koji Fujimoto², Kaori Togashi²

¹Tokyo University of Agriculture and Technology, Tokyo, Japan

50010645222@st.tuat.ac.jp {simiz, kobatake}@cc.tuat.ac.jp

²Kyoto University, Kyoto, Japan

Abstract. This paper presents a novel graph-cuts algorithm that can take into account a multiple-shape constraint and reports a lung segmentation process from a three-dimensional computed tomography (CT) image, based on the graph-cuts algorithm. A major contribution of this paper is the proposal of a segmentation algorithm that can consider multiple shapes in a graph-cuts framework. Using experiments, we demonstrate the effectiveness of the proposed multi-shape graph-cuts by comparing them to conventional single-shape graph-cuts using a synthetic image and clinical thoracic CT volumes.

Keywords: graph-cuts, multi-shape, fusion move, CT image, lung segmentation

1 Introduction

Accurate segmentation is a prerequisite for quantitative lung CT image analysis and also for computer-aided diagnoses. Many methods have been proposed to extract the lung regions automatically from three-dimensional (3D) CT volumes [1]. Since a normal lung appears dark in a CT image and is surrounded by denser regions, most methods focus on this contrast information. Although such methods are known to be simple and effective [2], they often fail to extract the region affected by pathologies.

For the segmentation of cases with pathologies, many approaches use the different features of lungs, rather than contrasts (e.g., using the shape of the lungs). Sluimer *et al.* proposed a registration-based approach in which a shape template was registered to an input CT volume [3]. They achieved significant improvements in the segmentation of lungs with pathologies, but the algorithm is time-consuming because of the combination of registration and classification processes. In addition, it suffers from a low accuracy in segmentation as a result of registration and classification errors. Hua *et al.* proposed a method that combines the classification process and a graph-search algorithm, and has been shown to be effective in cases containing pathologies [4]. However, the construction of the graph was limited to the narrow band around the pre-segmented lung surface obtained from the gray-value statistics-based method, which might fail in cases with a large pathology.

This paper proposes an s-t graph-cuts-based [5] segmentation algorithm with multiple shape priors, which can optimize an energy function defined in an entire CT

scan. A number of researchers have introduced a shape prior into a graph-cuts approach [6-8]. These papers show several ways to incorporate a general shape constraint, such as an ellipse, a star-shape, or an arbitrary shape defined by the user. A reference shape-based energy, computed by the Parzen window method, was proposed in [9]. The paper in [10] combined a patient-specific shape, estimated by a statistical shape model (SSM), with a graph-cut. However, all of the above methods consider single-shape information only, which might be different from the true shape, resulting in insufficient performance. Combining multiple-shape information will help to reduce such differences. A major contribution of this paper is the proposal of a graph-cuts-based segmentation algorithm that can consider multiple shapes. In the remainder of this paper, we will explain the details of our method and demonstrate its effectiveness using the experimental results of a synthetic image and thoracic CT volumes in clinical medicine.

2 Proposed Segmentation Framework

2.1 Single-shape graph-cuts

Graph-cuts formulate a segmentation problem as an energy minimization problem [5]. Given a set of voxels, P , and a set of labels, L , the goal is to assign a label $l \in L$ to each $p \in P$. Let A_p denote a label assigned to voxel p , and let $A = \{A_1, A_2, \dots, A_p, \dots, A_{|P|}\}$ be a collection of all label assignments. This gives the energy function:

$$E(A) = \lambda R(A) + B(A) = \lambda \sum_{p \in P} R_p(A_p) + \sum_{\{p,q\} \in N} B_{p,q} \delta_{A_p \neq A_q} \quad (1)$$

There are two types of energy terms in equation (1). The first term is called a data term, which expresses a penalty for assigning label A_p to voxel p . Generally, we use the negative log likelihood of the gray value for this term. The second term, $B_{p,q}$, is called a boundary term. This term expresses a penalty for assigning labels A_p and A_q to the two neighboring voxels, p and q . Originally, this term relies on a gradient value between voxels p and q . The set N is a collection of neighboring voxel pairs. The function δ is 1 if $A_p \neq A_q$, and 0 otherwise. The coefficient λ in the equation is a constant value balancing the two terms. In the following paragraphs, we briefly review the method of [10], which uses “single-shape graph-cuts”.

One of the contributions of [10] was the proposal of an energy term that can penalize the segmentation boundary based on a patient-specific shape, a priori. The following shape-constrained term, $S_{p,q}$, was introduced in the boundary term:

$$E(A) = \lambda \sum_{p \in P} \{R_p(A_p) + NB_p(A_p)\} + \sum_{\{p,q\} \in N} \{B_{p,q} + S_{p,q}\} \delta_{A_p \neq A_q} \quad (2)$$

$$S_{p,q} = \sqrt{[1 - \cos(\theta)]/2} \quad (3)$$

where θ represents an angle between a vector connecting voxels p and q and a gradient vector of a signed distance $\phi(p)$ from the boundary of given shape, a priori.

This term encourages the energy to be low when the direction of a vector connecting p and q is similar to that of the gradient vector of $\varphi(p)$. As a result, the surface normals of an extracted region tend to be parallel to those of the given shape. Thus, the extracted region is similar to the shape given to the algorithm.

Although the shape-constrained energy term $S_{p,q}$ has been shown to be effective, the algorithm still suffers from low accuracy, especially with test data. A patient-specific shape prior was estimated using an SSM beforehand. The estimation process works quite well for most cases, but it is still a challenging problem when dealing with test data in which an organ's shape is different from that in a training dataset. Therefore, there is a risk when using only a single shape. In this case, a collection of multiple shapes could account for the shape in a test dataset. This is why we propose a framework that can take into account multiple shape constraints.

$NB_p(A_p)$ in equation (2) is a neighbor-constrained term defined by the distance from the dorsal ribs. Since the lungs are surrounded by ribs, the term shows that regions inside and near the ribs are more likely to belong to the lungs.

2.2 Multi-shape graph-cuts

This section presents a graph-cuts-based segmentation algorithm that can solve the problem of a combination of multiple shape priors. Unlike a conventional graph-cuts algorithm, which deals with a binary label problem, we now consider multiple-shape priors, or multiple labels. Let a set, L , be a label set $\{0, 1, 2, \dots, n\}$ in which each label corresponds to a prior shape. Fig. 1 shows examples of labels, each with its original shape. Our goal is to develop an algorithm that will select an optimal shape at each voxel by minimizing an energy function, including the shape energy, of equation (4).

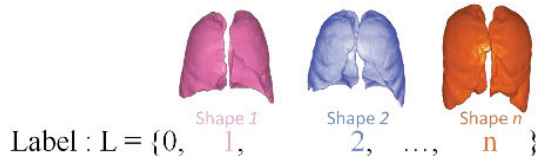


Fig. 1. A set of labels with their corresponding shapes.

$$E_{\text{shape}} = \sum_{(p,q) \in N} S_{p,q} \delta \quad (4)$$

$$S_{p,q} = \text{MIN}(\sqrt{[1 - \cos(\theta_{Ap})]/2}, \sqrt{[1 - \cos(\theta_{Aq})]/2})$$

where θ_{Ap} represents an angle between a vector connecting voxels p and q and a gradient vector of a signed distance φ_{Ap} (p) from the boundary of a shape corresponding to a label $A_p \in L$. Here, δ is a function that equals 0 when the neighboring voxels belong to same class, and 1 otherwise. Note that there are two classes, a lung ("object") class and background class in our problem.

Ideally, it is best to solve multi-label problems in one step. However, there is no algorithm that can handle problems in this manner. Instead, researchers use an

approximation algorithm that employs an iterative scheme, such as alpha-expansion [11] or fusion move [12]. These methods sequentially propose a label against a current label at each voxel. An important difference between the two algorithms is that the fusion move algorithm can propose different labels according to locations in each iteration, but the alpha-expansion algorithm cannot. As explained below, our algorithm proposes labels that differ by location so as to ensure the sub-modularity of the shape energy of equation (4). Consequently, we employ the fusion move algorithm, which iteratively solves a series of problems between a set of current labels and a set of proposed labels using the QPBO min-cut algorithm [13].

Let X^{cur} be a collection of current labels and X^{pro} be a set of proposed labels. Note that both X^{cur} and X^{pro} include multiple labels, each of which corresponds to an original shape. In order to ensure the sub-modularity of the shape energy, we divided the current labels into object labels and background labels. First, the fusion move algorithm proposes an “object” label, l , against voxels whose current labels, X^{cur} , are “background”, and proposes the same labels as current for other voxels ($X^{pro} \leftarrow X^{cur}$). The QPBO min-cut algorithm can find a combinatorial optimal solution of labels, or shape. This step can reduce false negatives, but cannot deal with false positives. The second step focuses on false positives, based on the same analogy. It proposes a “background” label l against voxels whose current labels X^{cur} are “object”. To compute the shape energy $S_{p,q}$ in the case of a background proposal, we extend the set of labels L to $L = \{1, -1, 2, -2, \dots, n, -n\}$, where the absolute value of a label refers to the number of a shape, and its sign represents the state of a voxel. Here, positive labels represent “object” labels and negative labels represent “background” labels. The QPBO min-cut algorithm can again find combinatorial optimal solutions of labels. We iterate a pair of object proposals and background proposals by changing a label, or a shape. The algorithm stops the iteration process when no label changes or when it reaches the maximum number of iterations defined by the user. Our method is summarized in Algorithm 1 and the differences over the single-shape graph-cuts are listed in Table 1.

Algorithm 1. Multi-shape graph-cuts

Input: a set of labels L , X^{cur}

Result: segmented regions

Initialize $X^{cur} = \{-1, \dots, -1\}$

Repeat

for each $l \in L$ **do**

Generate a set of labels X^{pro} where either l or an element of X^{cur} is assigned at each voxel

$X^{cur} \leftarrow X^{cur} \odot X^{pro}$ \odot : fusion move operator [12]

end for

until Convergence: no label changes or reaches maximum number of iterations

Prior to executing the proposed algorithm, we must decide a total number and an order of proposal of shape priors. As with the single-shape graph-cuts, patient-specific shape priors are estimated by combining an SSM and a pre-segmented result that is obtained by thresholding and morphological operations. Shapes similar to a pre-segmentation result are extracted from an eigen shape space. Actually, the top n shapes with a minimum distance between a shape in an eigen shape space and a

pre-segmented region are selected as the shape priors and used in the proposed multi-shape graph-cuts.

Table 1. Differences between a single-shape and multi-shape graph-cuts.

	Single-shape	Multi-shape
Number of shapes	1	n
Labels in A	binary	multiple labels ($2n$)
“Object” label(s)	1	$\{1, 2, \dots, n\}$
“Background” label(s)	0	$\{-1, -2, \dots, -n\}$

Finally, we will give an intuitive proof of the following inequality [12] to show the sub-modularity of the proposed energy term:

$$f_{pq}(X_p^{\text{cur}}, X_q^{\text{cur}}) + f_{pq}(X_p^{\text{pro}}, X_q^{\text{pro}}) \leq f_{pq}(X_p^{\text{cur}}, X_q^{\text{pro}}) + f_{pq}(X_p^{\text{pro}}, X_q^{\text{cur}}) \quad (5)$$

where X_p^{cur} is a current label and X_p^{pro} is a proposed label at voxel p , and f_{pq} means $S_{p,q} \cdot \delta$.

Proof. There are three cases with different signs of the product of X_p^{cur} , X_q^{cur} and the proposal label $l \in L$, where the three cases are mutually exclusive events and together cover all possible events. Note that a product of two labels is positive if the labels belong to the same class and negative otherwise.

Case 1: $X_p^{\text{cur}} \cdot X_q^{\text{cur}} > 0$

$f_{pq}(X_p^{\text{cur}}, X_q^{\text{cur}}) = f_{pq}(X_p^{\text{pro}}, X_q^{\text{pro}}) = 0$, because of the function δ . Therefore, we can write equation (5) as (5)', as follows:

$$0 + 0 \leq f_{pq}(X_p^{\text{cur}}, X_q^{\text{pro}}) + f_{pq}(X_p^{\text{pro}}, X_q^{\text{cur}}) \quad (5)'$$

Since f_{pq} is greater than or equal to 0, the above inequality is always met.

Case 2: $X_p^{\text{cur}} \cdot X_q^{\text{cur}} < 0$ and $X_p^{\text{cur}} \cdot l > 0$

Since X_p^{cur} belongs to the same class as proposal label l , $X_p^{\text{pro}} \leftarrow X_p^{\text{cur}}$.

Since X_q^{cur} belongs to a different class from proposal label l , $X_q^{\text{pro}} \leftarrow l$.

Therefore, we can write equation (5) as (5)'', which is an algebraic identity.

$$f_{pq}(X_p^{\text{cur}}, X_q^{\text{cur}}) + f_{pq}(X_p^{\text{cur}}, l) = f_{pq}(X_p^{\text{cur}}, l) + f_{pq}(X_p^{\text{cur}}, X_q^{\text{cur}}) \quad (5)''$$

Case 3: $X_p^{\text{cur}} \cdot X_q^{\text{cur}} < 0$ and $X_p^{\text{cur}} \cdot l < 0$

Since X_p^{cur} belongs to a different class from proposal label l , $X_p^{\text{pro}} \leftarrow l$.

Since X_q^{cur} belongs to the same class as proposal label l , $X_q^{\text{pro}} \leftarrow X_q^{\text{cur}}$.

Therefore, we can write equation (5) as (5)''', which is also an algebraic identity.

$$f_{pq}(X_p^{\text{cur}}, X_q^{\text{cur}}) + f_{pq}(l, X_q^{\text{cur}}) = f_{pq}(X_p^{\text{cur}}, X_q^{\text{cur}}) + f_{pq}(l, X_q^{\text{cur}}) \quad (5)'''$$

QED.

2.3 Energy function used in a lung segmentation process

This section explains the energy function used in this study. Although the proposed shape energy plays an important role in segmentation, it is not enough to extract the whole lung area precisely from a CT volume. As a conventional graph-cuts algorithm, a likelihood-based regional term, $R_p(A_p)$, a neighbor-constrained term, $NB_p(A_p)$ [10], a statistical atlas-based energy, $Atlas_p(A_p)$, as well as a boundary term, $B_{p,q}$ are combined with the proposed multi-shape energy.

$$\begin{aligned} E(A) = & \lambda \sum_{p \in P} \{R_p(A_p) + Atlas_p(A_p) + NB_p(A_p)\} \\ & + \sum_{\{p,q\} \in N} \{B_{p,q} + S_{p,q}\} \delta_{A_p \cdot A_q < 0} \end{aligned} \quad (6)$$

$$\begin{aligned} R_p(A_p) = & -\log(\Pr(I_p | "obj")) \text{ (if } A_p > 0) \\ R_p(A_p) = & -\log(\Pr(I_p | "bkg")) \text{ (if } A_p < 0) \end{aligned} \quad (7)$$

$$\begin{aligned} Atlas_p(A_p) = & 1.0 - P_{\text{atlas}}(p) \quad (\text{if } A_p > 0) \\ Atlas_p(A_p) = & P_{\text{atlas}}(p) \quad (\text{if } A_p < 0) \end{aligned} \quad (8)$$

$$\begin{aligned} NB_p(A_p) = & 0 \quad (\text{if } A_p > 0) \\ NB_p(A_p) = & D_{\text{rib}} \quad (\text{if } A_p < 0) \end{aligned} \quad (9)$$

where $P_{\text{atlas}}(p)$ represents the prior probability of the lungs at voxel p calculated from training data. The function δ for boundary terms is defined as below.

$$\begin{aligned} \delta_{A_p \cdot A_q < 0} = & 1 \text{ (if } A_p \cdot A_q < 0) \\ \delta_{A_p \cdot A_q < 0} = & 0 \text{ (if } A_p \cdot A_q > 0) \end{aligned} \quad (10)$$

Since positive labels represent an “object” class and negative labels represent a “background” class, the basic function of the equation is essentially the same as δ in equation (1).

3 Experimental Evaluations

3.1 Materials

Synthetic image: A 2D synthetic image [10] was used for performance validation (Fig. 2(c)). The image includes not only an object (Fig. 2(a)), but also noises consisting of six structural noises (Fig. 2(b)) and an additive Gaussian noise ($N(0, 20^2)$) (Fig. 2(c)). The structural noises mimic lesions and vessels with different

contrasts in an organ. The radius of the object in Fig. 2(a) is 40 [pixel] on average, and the amplitude, A, is 5 [pixel]. The distance dx and dy refer to the displacement of an object in the shape templates that were used as shape priors. In this experiment, we changed the amplitude A and distances dx and dy of the shape template to incorporate various deviations from the true shape. We used uniform random numbers for the parameters A, dx, dy ($A: [5, 10]$, $dx: [-10, -5]$, $dy: [5, 10]$), and generated 10 shape priors, as shown in Fig. 2(d). For the boundary term of the energy function, we employed an eight-neighborhood system for this experiment.

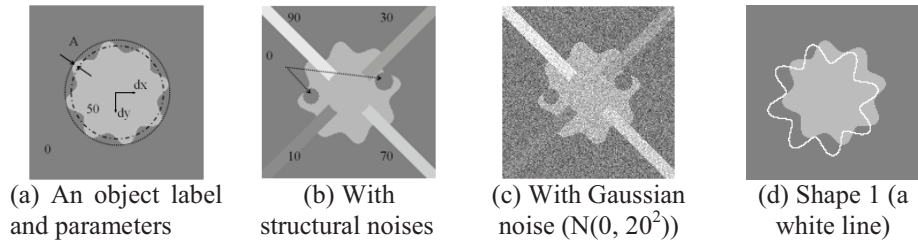


Fig. 2. Illustrations for a synthetic image (150×150). Numerals in (a) and (b) are gray values of objects.

Table 2. Parameters of the shape priors.

Parameter	1	2	3	4	5	6	7	8	9	10
A	8	6	5	7	8	7	8	9	7	7
dx	9	8	-8	-7	-6	-10	-8	8	-7	9
dy	-7	8	8	-6	-8	-7	6	-7	-9	-9

Clinical CT volumes: We performed lung segmentation using 97 cases with pulmonary diseases, such as lung carcinoma. These cases include both non-contrast and contrast CT volumes (image size: $512 \times 512 \times 204\text{--}561$ [voxel], pixel size: $0.625\text{--}0.741$ [mm/pixel], slice spacing: 0.5–1.0 [mm], bits stored: 16 [bit]). In this experiment, we included the lungs and the regions of pleural effusion as target objects for segmentation. It is worth noting that all the processes are 3D automated. We employed a 26-neighborhood system for the graph-cuts. We divided the data into 49 training and 48 test data sets and the performance of the algorithm was assessed by a holdout validation test. The training data were used for building a shape model (a level set distribution model (LSDM) [14]), which is based on a signed distance map from the contour of a shape. The data were also used to build a probabilistic atlas for energy $\text{Atlas}_p(A_p)$ and to calculate gray-value statistics of the lungs and other regions for energy $R_p(A_p)$. In order to estimate patient-specific shape priors, we calculated a Jaccard Index (J.I.) as a metric to compute the distance between a pre-segmented region and the shapes in an eigen space. Specifically, we first projected the pre-segmented result to the eigen space, which has a 95% contribution rate, and picked the top five shapes close to the projection point. The shapes were generated by discretizing the eigen-shape space with 1σ spacing from an average shape and a range of $\pm 2\sigma$. We determined the parameters λ and σ in the energy function from

experiments so that the average sensitivity of pathological regions in lung areas was 90%.

3.2 Results

Synthetic Image: This experiment showed the effectiveness of $S_{p,q}\delta$ directly by minimizing equation (6) without $\text{Atlas}_p(A_p)$ and $\text{NB}_p(A_p)$. The resultant images are shown in Fig. 3(c). Fig. 4 displays the number of iterations vs. J.I. between the extracted regions and the true regions, and the number of iterations vs. total energy of the equation.

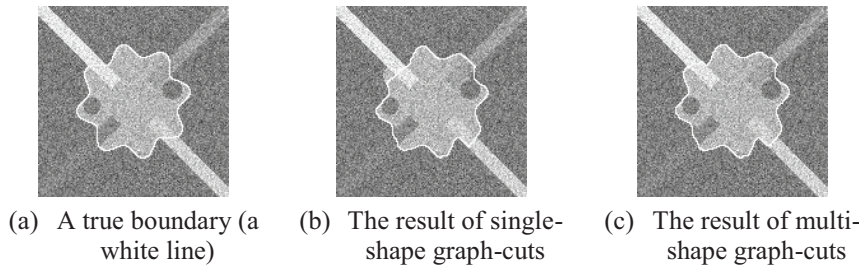


Fig. 3. Segmentation result of a synthetic image.

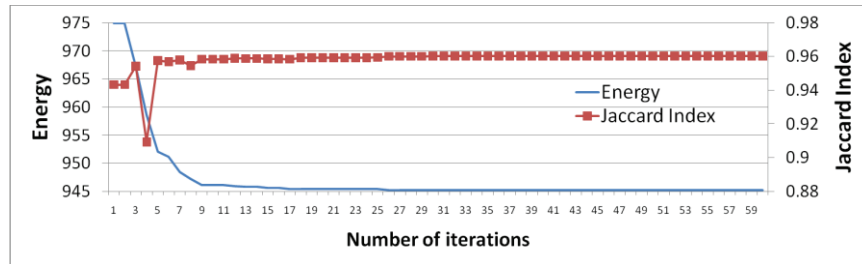


Fig. 4. Number of iterations vs. energy and segmentation performance.

In Fig. 4, the total energy was monotonically decreasing, and J.I. tended to increase as the energy decreased. Specifically, J.I. increased from 0.943 to 0.960. The first J.I. shows the performance of single-shape graph-cuts (Fig. 3(b)), and the last J.I. shows that of the proposed multi-shape graph-cuts (Fig. 3(c)). It was confirmed from these results that the multi-shape graph-cuts could reduce segmentation errors by considering multiple shapes.

Clinical CT volumes: This experiment minimized equation (6). Figs. 5(a)–(c) show cases in which the single-shape graph-cuts were inferior to the proposed method as a result of false positives of the heart region, as indicated by an arrow. In order to evaluate the results quantitatively, we computed an average distance between an extracted surface and a manually delineated surface. The average distance of this case was improved from 0.835 to 0.523 [mm]. Figs. 5(d)–(f) show failure cases, using both

methods, in which the average distances are 0.862 [mm] for the single-shape graph-cuts and 0.732 [mm] for the multi-shape graph-cuts. Figs. 6(a)–(c) show examples of segmentation results of cases that contain pathologies. Because we tuned our graph-cuts parameters to obtain an average sensitivity of 90%, in most cases, these lesions were extracted correctly as part of the lungs. Fig. 7 shows the average and standard deviation of the average distance over all testing data, which was improved from 0.719 ± 0.309 to 0.587 ± 0.176 [mm]. The Wilcoxon test told us that the difference was statistically significant, with a risk of $p < 0.01$.

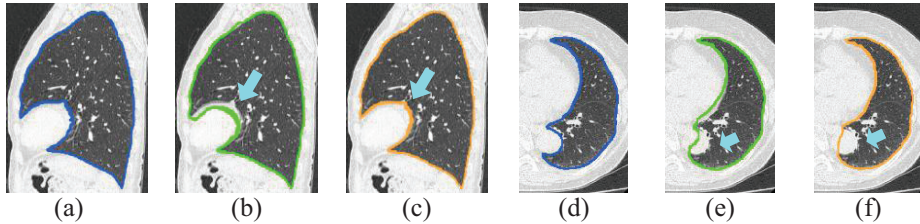


Fig. 5. Examples of segmentation results. (a) and (d): true boundaries, (b) and (e): single-shape graph-cuts, (c) and (f): multi-shape graph-cuts.

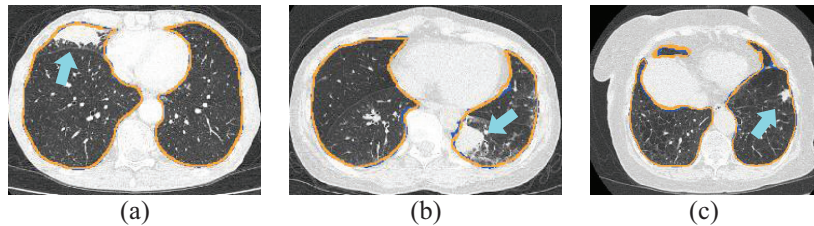


Fig. 6. Examples of segmentation results of cases containing pathologies. Blue lines: true boundaries; orange lines: resultant boundaries from the multi-shape graph-cuts.

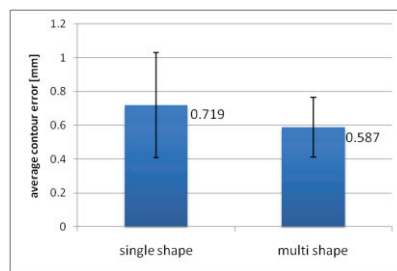


Fig. 7. Performance index of single-shape graph-cuts and multi-shape graph-cuts: average and standard deviation of testing 48 clinical cases.

4 Discussion

Synthetic Image: Fig. 8 shows the segmentation results of the fourth and fifth iterations with their shape priors. Here, the performance changed rapidly during the iterations, as we can see in Fig. 4. The fourth iteration (proposal of “background” with second shape a priori) generated significant false negatives, as indicated by an arrow, as a result of the improper shape of (a). The result was a rapid decrease of the J.I. However, when the third shape a priori of (c), which is more similar to the true shape in terms of gradient vector distribution, was proposed, the multi-shape graph-cuts succeeded in extracting the region. The remaining iterations kept the shape of (d). The false negatives of (b) never recurred because the energy of (d) is smaller than that of (b). From the above, we concluded that if an appropriate shape prior that is similar to the true shape is included in a set of proposed shapes, our algorithm can combine the shapes appropriately, resulting in higher accuracy in segmentation than with single-shape graph-cuts.

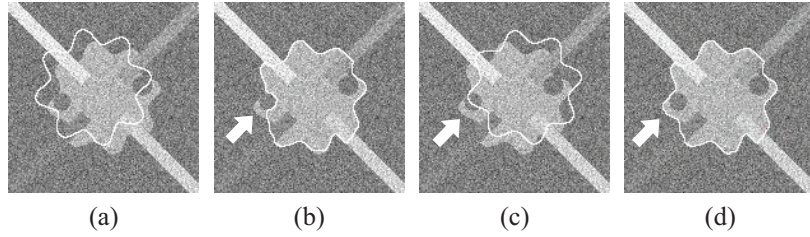


Fig. 8. Shape a priori and the segmentation results of fourth and fifth iterations: (a) the shape a priori of the fourth iteration (“background” proposal), (b) the result of the fourth iteration, (c) the shape a priori of the fifth iteration (“object” proposal), and (d) the result of the fifth iteration.

Clinical CT volumes: As presented in the results of clinical CT volumes in section 3, the multi-shape graph-cuts is statistically superior to the single-shape graph-cuts, while maintaining high sensitivity to lesions. Fig. 9(a) is a first shape prior, which differs from the true shape of the heart, resulting in the segmentation error of Fig. 5(b). However, the fourth shape a priori of Fig. 9(d), which is similar to the true shape, improved the segmentation performance (see Fig. 5(c) for segmentation result).

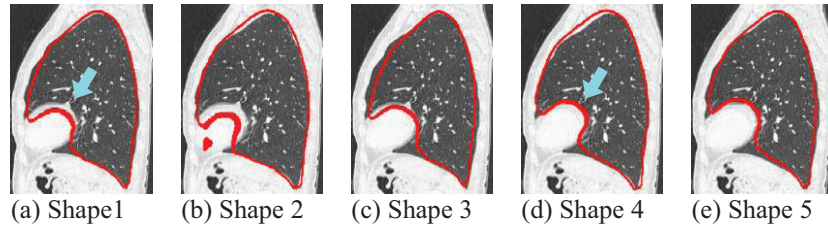


Fig. 9. Shape priors used for the case in Figs. 6(a)–(c).

Fig. 10 presents the shape priors of Figs. 5(d)–(f). Since the shape of the aorta region of this case is unique and differs from those of SSM training data, it was

impossible to estimate the shape correctly. Consequently, there was no shape among the set of proposed shapes that resembled the aorta. The failure of Figs. 5(e) and (f) could be explained by the above reasons.

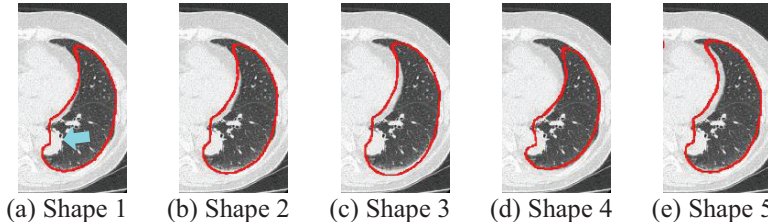


Fig. 10. Shape priors used for the case in Figs. 6(d)–(f).

5 Conclusion

This paper proposed a novel graph-cuts algorithm that can take into account a multiple-shape constraint. A salient feature of our method is that it can choose an optimal shape *a priori* at each voxel by combining the proposal of multiple priors with the fusion move algorithm. The algorithm sequentially proposed multiple labels, each of which corresponds to a shape prior, and minimized the energy function by the QPBO min-cut algorithm, which guarantees the global optimum in each iteration.

Using experiments, we demonstrated and discussed the effectiveness and limitations of our method using a synthetic image and 97 clinical CT volumes. The first experiment used a synthetic image to present the effectiveness of using multiple shapes. Secondly, a holdout validation test of clinical CT volumes showed that our method improved the average distance over all testing data from 0.719 ± 0.309 to 0.587 ± 0.176 [mm], which was statistically significant ($p < 0.01$, Wilcoxon test). The computational time of our algorithm was approximately 30 min per CT volume (Intel(R) Core(TM) i7 3.07 GHz \times 2).

In future work, we will construct algorithms that provide proper shape priors and optimize the number of priors. We will also conduct further experiments in the near future with cases of severe pathologies, followed by an improvement of the shape energy. Lastly, we plan to apply the multi-shape graph-cuts to another segmentation problem, such as multi-organ segmentation from medical imagery.

References

1. Sluimer, I., Schilham, A., Prokop, M., van Ginneken, B.: Computer analysis of computed tomography scans of the lung: a survey. *IEEE TMI*, 25, 4, pp.385-405 (2006).
2. Hu, S., Hoffman, E.A., Reinhardt, J.M.: Automatic lung segmentation for accurate quantitation of volumetric X-ray CT images. *IEEE TMI*, 20, 6, pp.490-498 (2001).
3. Sluimer, I., Prokop, M., van Ginneken, B.: Toward automated segmentation of the pathological lung in CT. *IEEE TMI*, 24, 8, pp.1025-1038 (2008).

4. Hua, P., Song, Q., Sonka, M., Hoffman, E. A., Reinhardt, J.M.: Segmentation of pathological and diseased lung tissue in CT images using a graph-search algorithm. ISBI, pp.2072-2075 (2011).
5. Boykov, Y., Funka-Lea, G.: Graph cuts and efficient N-D image segmentation. IJCV, 70, 2, pp.109-131 (2006).
6. Slabaugh, G., Unal, G.: Graph cuts segmentation using an elliptical shape prior. Proc. Of ICIP, 2, pp.1222-1225 (2005).
7. Funka-Lea, G., Boykov, Y., Florin, C., Jolly, M., Moreau-Gobard, R., Ramaraj, R., Rinck, D.: Automatic heart isolation for CT coronary visualization using graph-cuts. ISBI, pp.614-617 (2006).
8. Freedman, D., Zhang, T.: Interactive graph cut based segmentation with shape priors. CVPR, 1, pp.755-762 (2005).
9. Linguraru, M.G., Pura, J.A., Chowdhury, A.S., Summers, R.M.: Multi-organ segmentation from multi-phase abdominal CT via 4D graphs using enhancement, shape and location optimization. MICCAI, 6363, pp.89-96 (2010).
10. Shimizu, A., Nakagomi, K., Narihira, T., Kobatake, H., Nawano, S., Shinozaki, K., Ishizu, K., Togashi, K.: Automated segmentation of 3D CT images based on statistical atlas and graph cuts. MICCAI-MCV, pp.127-138 (2010).
11. Boykov, Y., Veksler, O., Zabih, R.: Efficient approximate energy minimization via graph cuts. TPAMI, 23, 11, pp.1222-1239 (2001).
12. Lempitsky, V., Rother, C., Roth, S., Blake, A.: Fusion move for Markov random field optimization. IEEE TPAMI, 32, 8, pp.1392-1405 (2010).
13. Rother, C., Kolmogorov, V., Lempitsky, V., Szummer, M.: Optimizing binary MRFs via extended roof duality. CVPR, pp.1-8 (2007).
14. Leventon, M.E., Grimson, W.E.L., Faugeras, O.: Statistical shape influence in geodesic active contours. CVPR, 1, pp.316-323 (2000).